External Drivers and Mesoscale Self-Organization of Shallow Cold Pools in the Trade-Wind Regime

Alinaghi, Pouriya; Siebesma, A. Pier; Jansson, Fredrik; Janssens, Martin; Glassmeier, Franziska

External Drivers and Mesoscale Self-Organization of Shallow Cold Pools in the Trade-Wind Regime

Pouriya Alinaghi[1] , A. Pier Siebesma[1,2], Fredrik Jansson[1] , Martin Janssens[1,3] , and Franziska Glassmeier[1]

[1]Department of Geoscience & Remote Sensing, Delft University of Technology, Delft, The Netherlands, [2]R & D Weather and Climate Models, Royal Netherlands Meteorological Institute (KNMI), De Bilt, The Netherlands, [3]Department of Meteorology & Air Quality, Wageningen University & Research, Wageningen, The Netherlands

Abstract Recent observations of the trade-wind regions highlight the covariability between cold-pool properties and mesoscale cloud organization. Given the covariability of organization with cloud cover and albedo, this suggests a potential impact of cold pools on the cloud radiative effect (CRE). To explore this, we use an ensemble of 103 large-domain, high-resolution, large-eddy simulations and investigate how the variability in cold pools is determined by large-scale external cloud-controlling factors and shaped by processes within the mesoscale. It is demonstrated that the size and frequency of occurrence of cold pools are strongly influenced by the near-surface horizontal wind speed and large-scale subsidence. The temporal evolution of cold pools is strongly correlated with the diurnality in radiation. Even without external variability, we find a strong intermittent behavior in the evolution of cold pools, governed by a complex interplay between cold pools and clouds which expresses itself in the form of shallow squall lines. These squall lines result from precipitating downdrafts, cold pool outflows and the resulting gust fronts, reinforcing parent clouds. Cold pools influence the CRE of trade cumuli, but only when they exist during the day. This emphasizes the importance of the synchronization between cold-pool events and the diurnal cycle of insolation for the dependence of the CRE on cold pools.

Plain Language Summary Mesoscale cloud patterns of trade cumuli are important for their radiative effects. Therefore, understanding the processes patterning these clouds is essential. Recent observations show that cold pools, resulting from rain evaporation, covary with mesoscale patterns in the trades. To understand the significance of cold pools, we investigate the extent to which they respond to large scales. We employ an ensemble of large-eddy simulations, capable of resolving processes associated with cumulus cloud formation. We find that cold pools are predominantly controlled by large-scale conditions. The evolution of cold pools is influenced by the diurnal cycle of radiation. We also explore how cold pools–independently of external forcing–evolve and interact with clouds. We find that the cold-pool evolution shows intermittent behavior, driven by complex interactions with clouds. This interaction expresses itself as shallow squall lines, consisting of precipitating downdrafts, diverging outflows, and converging updrafts at cold-pool gust fronts, reinforcing the parent clouds, and thereby cold pools affect cloud-radiative effect (CRE). However, to substantially impact CRE, cold pools must exist during daytime. Our findings improve our understanding of the mesoscale processes through which trade cumuli organize and how those processes respond to large scales, which is a step toward constraining trade-cumulus climate feedback.

1. Introduction

Cold pools are pockets of cold dense air that result from downdrafts associated with rain evaporation in the sub-cloud layer. When these downdrafts reach the surface, they expand circularly, forming mesoscale cloud arcs visible in satellite imagery (Zuidema et al., 2012, 2017). The local impact of cold pools is evident in both shallow and deep convection and consists of significantly altering the sub-cloud layer's thermodynamic structure and dynamics (e.g., Böing et al., 2012; Drager & van den Heever, 2017; Lochbihler et al., 2021; Schlemmer & Hohenegger, 2016; Touzé-Peiffer et al., 2022; Vogel et al., 2021; Zuidema et al., 2012). Cold pools suppress the convection underneath clouds but can trigger new convective events by accumulating heat and moisture while maintaining a relatively higher wind speed at cold-pool fronts (e.g., Jeevanjee & Romps, 2013; Langhans & Romps, 2015; Tompkins, 2001; Torri et al., 2015; Vogel et al., 2021; Zuidema et al., 2012). When cold-pool fronts collide, they can even more forcefully trigger new convection, a feature described in the deep

Project administration:
A. Pier Siebesma, Franziska Glassmeier
Resources: Fredrik Jansson,
Martin Janssens, Franziska Glassmeier
Software: Pouriya Alinaghi,
Fredrik Jansson, Martin Janssens
Supervision: A. Pier Siebesma,
Franziska Glassmeier
Validation: Pouriya Alinaghi,
A. Pier Siebesma, Fredrik Jansson,
Martin Janssens, Franziska Glassmeier
Visualization: Pouriya Alinaghi
Writing – original draft:
Pouriya Alinaghi, A. Pier Siebesma
Writing – review & editing:
Pouriya Alinaghi, A. Pier Siebesma,
Fredrik Jansson, Martin Janssens,
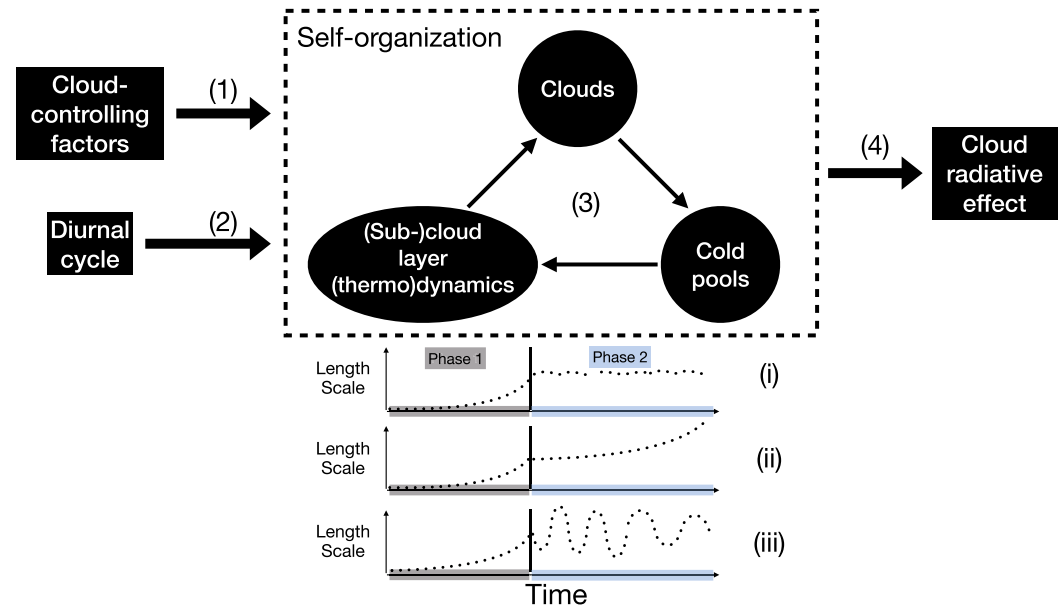Franziska Glassmeier

Figure 1. A conceptual picture of the trade-cumulus cloud system. The dashed rectangle box shows the trade cumulus system which is forced by (1) the large-scale CCFs and (2) the diurnal cycle. Having time-invariant and conducive CCFs, this system shows (3) self-organization via interaction between its components, that is, clouds and cold pools. As a result of these interactions, this system might show (i) a time-invariant, (ii) an unstable, or (iii) an intermittent behavior. The resulting (4) cloud-radiative effect is expected to depend on the details of links (1) to (3).

convective regime (Torri & Kuang, 2019) as well as in shallow cumulus (Xue et al., 2008) and open-cell stratocumulus (Savic-Jovcic & Stevens, 2008). In these cases, such mutual interactions between cold pools give rise to a self-organization of the cloud fields that manifests in horizontal variability on the mesoscale (Glassmeier & Feingold, 2017; Haerter et al., 2019; Nissen & Haerter, 2021). Due to their interaction with ambient environmental shear, which invigorates and sustains the convection, cold-pool fronts can also evolve into squall lines, not only in deep convective systems (Moncrieff & Liu, 1999; Rotunno et al., 1988; Weisman & Rotunno, 2004), but also in case studies of shallow trade cumulus fields (Dauhut et al., 2023; Li et al., 2014).

Recent research on the climatology of trade-cumulus cold pools shows that the subjectively identified cloud patterns–*Sugar*, *Gravel*, *Flowers*, *Fish* (Stevens et al., 2020)—have distinct cold-pool statistics (Vogel et al., 2021). Given the effect of mesoscale cloud organization on cloud radiative effect (CRE) through its correlation with both cloud cover (Bony et al., 2020) and albedo (Alinaghi et al., 2024; Denby, 2023), these findings suggest that cold pools likely play a significant role in regulating the radiative effect of shallow cumulus clouds in the trades. However, the response of CRE to cold pools in the trades has not yet been directly explored. Therefore, this study aims to understand how cold pools can influence CRE. As illustrated in Figure 1, this implies investigating (i) the underlying mechanisms through which cold pools evolve and interact with trade-cumulus clouds for fixed large-scale conditions, that is, their self-organization on the mesoscale, and (ii) the extent to which this behavior is controlled by the large-scale conditions.

For large-scale conditions that are fixed in time and spatially homogeneous (dashed box in Figure 1), large-eddy simulations (LESs) of non-precipitating trade cumuli tend to self-aggregate into clustered structures (Bretherton & Blossey, 2017; Janssens et al., 2023; Narenpitak et al., 2021), leading to growth in their horizontal length scales (Phase 1 in the time series of Figure 1). Ultimately, the deepening alongside this increased clustering leads to the initiation of precipitation (Phase 2 in the time series of Figure 1). As a result of rain evaporation, cold pools develop spontaneously from such conditions over domains of 50–300 km^2 (e.g., Anurose et al., 2020; Lamaakel et al., 2023; Seifert & Heus, 2013; Vogel et al., 2016). Formation of cold pools, in turn, leads to the presence of ring-like structures at the mesoscales. Throughout the manuscript, we use the term *self-organization* for the precipitating cumulus system because (i) these ring-like structures form under large-scale conditions that are invariant in time and space, and (ii) the interactions between cold pools and clouds mutually organize themselves into these ring-like structures at the mesoscale. A recent realistically forced LES case study of the so-called

Flowers on 2 February 2020, highlighted the role of cold pools in shaping this pattern in shallow convection, similar to how deep mesoscale convective systems self-organize along squall lines thanks to cold pools dynamics (Dauhut et al., 2023). However, it remains unclear whether this "shallow squall line" analogy holds beyond this single case study. Thus, our first aim is to investigate the mechanisms through which cold pools in the trades self-organize and interact with clouds from their formation until their dissipation (Figure 1, link 3). We will specifically explore, whether length-scale growth stabilizes under cold-pool activity (Phase 2, Option i), keeps increasing (Phase 2, Option ii), or shows an intermittent behavior (Phase 2, Option iii).

The next question is whether and how these self-organized fields of cold pools in the trades are controlled by the large-scale conditions, or cloud-controlling factors (CCFs). Variations in CCFs can be expected to directly control variations in convective triggering among mesoscale airmasses, and thus control fields of self-organized cold pools (Figure 1, link 1). For example, forward shear is more effective than backward shear in triggering new cold-pool-driven convective events in LES experiments (Helfer & Nuijens, 2021). The diurnal cycle of insolation appears to consistently control characteristics of cold pools and their associated cloud patterns (Figure 1, link 2), cloud cover and precipitation in observations (Radtke et al., 2022; Vial et al., 2021; Vogel et al., 2021). Furthermore, cold-pool-coupled trade cumulus patterns (Vogel et al., 2021) can be classified by their large-scale surface wind speed and inversion strength (Bony et al., 2020, their Figure 3). Despite the expected response of trade-cumulus cold pools to CCFs, we do not yet know (i) the precise magnitude of this response, and (ii) which CCFs are the most important.

We comprehensively address these questions by means of a large ensemble of large-domain LESs. Such ensembles are becoming increasingly computationally feasible (Jansson et al., 2023). Their advantages compared to case studies lie not only in their greater generality but also in their amenability to statistical analyses, which facilitates model-measurement integration (Alinaghi et al., 2024; Chen et al., 2024; Feingold et al., 2016; Glassmeier et al., 2019; Gryspeerdt et al., 2022; Hoffmann et al., 2020, 2023; Mapes, 2024). We specifically employ the *Cloud Botany* data set, which includes 103 idealized, large-domain, LESs of shallow cumulus clouds (Jansson et al., 2023). These simulations were performed using the Dutch Atmospheric Large Eddy Simulation (DALES) model (Heus et al., 2010) and incorporate varying large-scale CCFs such as tropospheric stability, geostrophic wind, sea-surface temperature, and large-scale vertical velocity. The range of the used values of these CCFs are determined from ERA5 reanalysis data (Hersbach et al., 2020) and EUREC^{4}A field campaign (Bony et al., 2017; Stevens et al., 2021) and are therefore representative of the large-scale conditions of the trade-wind regions over the subtropical Northern Atlantic Ocean where cold pools frequently occur. This makes the *Cloud Botany* perfectly suitable for systematically exploring and categorizing the interplay between cold pools and the environmental conditions in which they form, develop, and decay.

In the remainder of the paper, we first introduce the data and methods, followed by a quantification of the response of cold pools to variations in large-scale CCFs (Figure 1, link 1, Section 3.1) as well as to the diurnal cycle of insolation (Figure 1, link 2, Section 3.2). To solely focus on the dependence of cold pools on self-organizing mechanisms (Figure 1, link 3), the diurnality in radiation is switched off in Section 3.3. We eventually present how the self-organization of cold pools manifests itself into 2D cloud patterns and how this affects CRE (Figure 1, link 4) in Section 3.4. We summarize our results in Section 4.

2. Methodology and Data

2.1. *Cloud Botany* Ensemble

The main data source for this study is the output of a large ensemble of LESs of shallow cumulus cloud fields, produced with the Dutch Atmospheric Large-Eddy Simulation (DALES) model (Jansson et al., 2023). This data set, called *Cloud Botany*, consists of 103 simulations, each 60 hr long, over $150 \times 150\text{-km}^2$ domains with a horizontal resolution of 100 m and a vertical resolution of 20 m (which stretches by 1% with height). The *Botany* simulations were run for a range of different idealized large-scale forcings and environments, controlled by six parameters; we will refer to these parameters as cloud-controlling factors (CCFs) (Jansson et al., 2023, their Figure 2). These CCFs are the sea-surface liquid-water potential temperature (θ_{l0}), near-surface geostrophic wind speed (u_0), the moisture scale height (h_{q_t}), the temperature lapse rate in the free troposphere (Γ), large-scale vertical velocity variability (w_1), and the shear in the horizontal geostrophic wind (u_z). Each simulation was

Table 1
Parameters of the Botany Ensemble

Large-scale and initial conditions	Parameters [units]	Ensemble's mean	Ensemble's standard deviation
Sea-surface liquid-water potential temperature	θ_{l0} [K]	299	0.84
Near-surface geostrophic wind speed	u_0 [m/s]	−10.6	3.65
Temperature lapse rate in the free troposphere	Γ [K/km]	5	0.51
The moisture scale height	h_{q_t} [m]	1,810	515
Large-scale vertical velocity variability	w_1 [cm/s]	0.0393	0.1906
Shear in the horizontal geostrophic wind	u_z [(m/s)/km]	2.22	1.79

Note. Overall statistics of the ensemble's parameters determining CCFs.

initialized with the profiles of temperature, humidity and wind that determine the large-scale environment. Table 1 provides information on the ensemble's mean and standard deviation of these CCFs.

The range of used values for the CCFs is based on the global ERA5 reanalysis data of the trade-wind environment (Hersbach et al., 2020). All *Botany* simulations feature constant large-scale tendencies for drying and cooling through advection as depicted by Jansson et al. (2023, their Figure 3). Additionally, diurnality in incoming solar radiation is incorporated throughout the entire *Botany* simulations. The cloud-droplet number concentration is fixed and equal to $70 \times 10^6/m^3$ in every grid cell of *Botany* simulations. For further details about the design and parameters of the *Botany* ensemble, we refer the readers to the data set paper (Jansson et al., 2023).

Each simulation member of the *Botany* ensemble is initialized from a homogeneous non-cloudy state, and the external CCFs are time-invariant throughout each simulation member. This means that the evolution of cloud fields is internally driven by, for example, the interactions between the components of system, that is, *self-organization*. This allows studying processes through which the system self-organizes. To illustrate their overall behavior, we show Figure 2a, which provides the time series of the domain-mean (cloud-)liquid-water path $\mathcal{L}$ and rain-water path $\mathcal{R}$ averaged over the entire ensemble. Figures 2b–2e further show the albedo contour plots of the central reference simulation at 5, 23, 29, and 54 hr after the starting time of the simulation. All simulations in the *Botany* ensemble start from a homogeneous non-cloudy state (Figure 2a). During the spin-up time of the first ≈ 10 hr, a majority of simulation members (87 out of 103) develop small cumuli (Figure 2b) that due to self-reinforcing shallow circulations (Janssens et al., 2023) clump together and deepen (Figure 2c). This marks phase 1 in Figure 1. Once these aggregated clouds deepen sufficiently, they begin to precipitate (≈ Hour 22; Figure 2a) and form cold pools. This marks the beginning of phase 2 shown in Figure 1. The cold pools can be visually diagnosed as relatively cloud-free areas surrounded by cloudy rings in Figures 2d and 2e. The simulated cloud rings and cold pools are sometimes topped by stratiform anvils (Figure 2d), which visually resemble *Flowers* (Stevens et al., 2020). Later, the cold pools organize into (semi-)cellular structures (Figure 2e), which resemble Stevens et al. (2020)'s *Gravel*. Cloudiness and precipitation grow through the night and peak at sunrise (Figure 2a). Afterward, due to the stabilizing effect of daytime shortwave radiative heating, cloudiness and precipitation decline until around sunset, where they start to grow again. As cold pools result from rain evaporation, all our analyses throughout this paper focus on the second day of the *Botany* simulations, where the cumuli robustly precipitate (Figure 2a), that is, phase 2 of Figure 1.

2.2. Cold Pools Diagnosed by the Mixed-Layer Height

Once clouds are raining, rain-evaporation cools the sub-cloud layer, while condensation warms the cloud layer, stabilizing the boundary layer. Consistently, cold pools in the trades often correspond to a drop in near-surface temperature (up to ≈ 1–2 K) and specific humidity (up to ≈ 1.5 g/kg), as observed by Zuidema et al. (2012). In this study, we diagnose cold pools using the (shallow) mixed-layer height (h_{mix}) from the 2D outputs of the *Botany* data set, which is calculated according to the method proposed by Rochetin et al. (2021, their Equation 1). The metric h_{mix} has been demonstrated as a reliable indicator for trade cumulus cold pools, with the area affected by cold pools exhibiting low values of h_{mix}, in both observations (Touzé-Peiffer et al., 2022) and models (Rochetin et al., 2021).
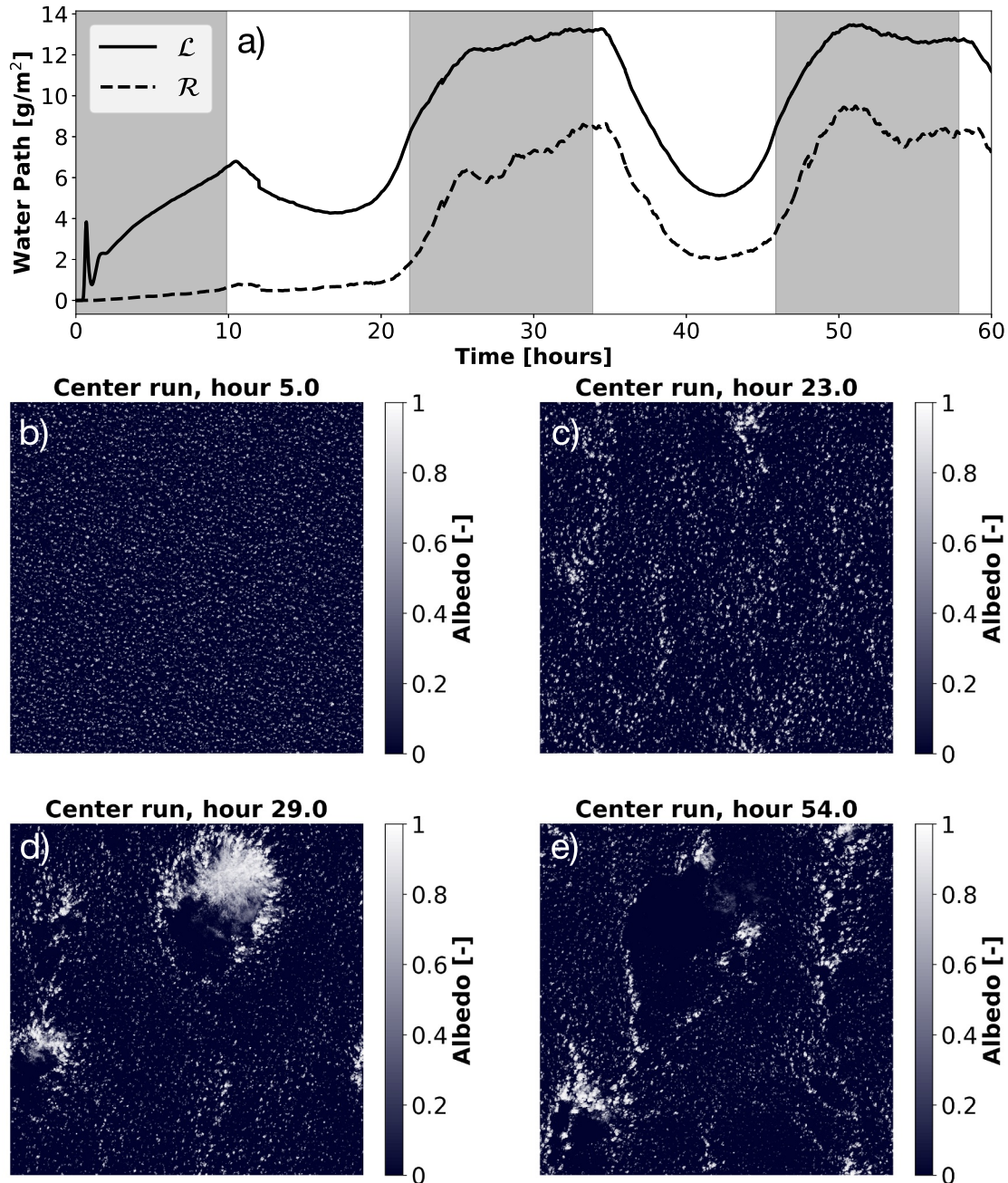
Figure 2. Evolution of cumulus clouds in *Botany*. (a) Time series of domain-mean liquid-water path ($\mathcal{L}$) and rain-water path ($\mathcal{R}$), averaged over the entire *Botany* ensemble. Gray-shaded areas correspond to nighttime. (b–e) Contour plots of cloud albedo for the central reference simulation (run 1) that has the mean CCFs of the entire ensemble.

To illustrate how we diagnose cold pools from the horizontal field of h_{mix}, consider the snapshot in Figure 3a. Figure 3b depicts the probability density distribution (PDF) of h_{mix} corresponding to Figure 3a. The ansatz for our diagnosis of a cold pool is to imagine a symmetric mono-modal distribution in this PDF that would have occurred in the absence of cold pools; in this field, its mode is around 900 m. We approximate the upper boundary of this distribution as the 99th percentile of the 2D h_{mix}. Next, we mark its lower boundary by subtracting the difference between the mode and the upper boundary from the mode (blue line in Figure 3b). Any pixel with an h_{mix} smaller than this height is considered a cold-pool pixel. The outline of the resulting cold-pool mask for this example is shown in Figure 3a.

Figure 3. Cold-pool mask definition. (a) Contour plot of h_{mix} for hour 29 of the central reference simulation, which its cloud field is shown in Figure 2. The cold-pool mask is shown by the green dashed contour line. (b) The probability density distribution of the h_{mix} shown in (a).

Using this cold-pool mask, we quantify spatial cold-pool characteristics, such as their fraction f_{cp}, number n_{cp}, and size $s_{cp} = \sum_{i=1}^{n_{cp}} \sqrt{A_i}/n_{cp}$, where A_i denotes the area o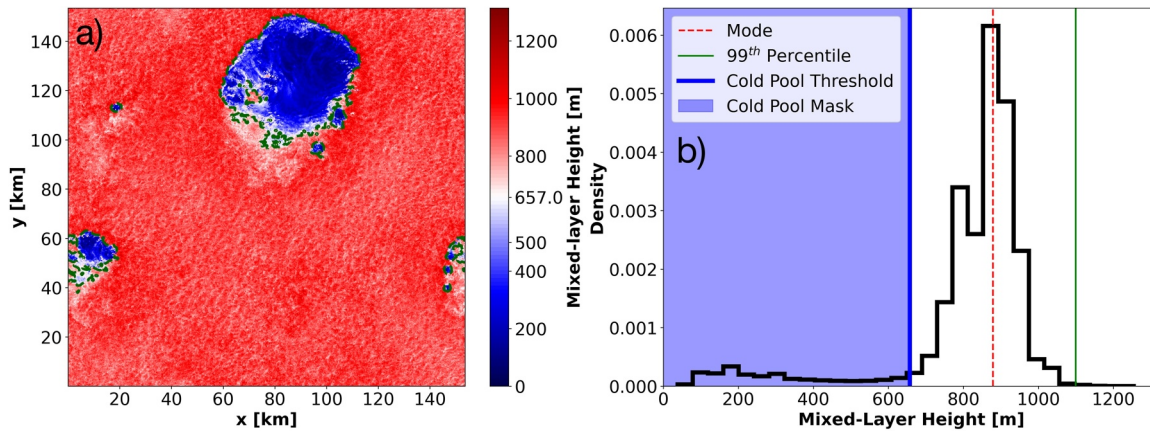f each individual cold-pool object within the simulation domain. Each cold-pool object is detected as 2D contiguous objects using the clustering technique. These metrics are calculated for all simulations every 5 minutes, which is the temporal resolution of the h_{mix} output in the *Botany* data set.

Like previous studies (e.g., Drager & van den Heever, 2017; Rochetin et al., 2021), there are statistical assumptions in defining cold pools. However, the main results are not sensitive to these definition details. For instance, using the condition $h_{mix} < 400$ m for defining cold pools, as proposed by Touzé-Peiffer et al. (2022), yields very similar results (see Section 3.1).

Lastly, to explore the interactions between cold pools and clouds throughout the paper, particularly in Sections 3.3 and 3.4, we use several cloud-field properties such as the domain-mean size of cloud objects (L_c), the mean fraction of open-sky areas (L_o) (Janssens et al., 2021), the domain-mean geometric thickness (h), and the domain-mean size of precipitation cells (L_p). The definitions of these metrics are detailed in the Supporting Information S1.

3. Results and Discussion

3.1. The Dependence of Cold Pools on Cloud-Controlling Factors

The dependence of cold pools on the CCFs (Figure 1, link 1) is analyzed using a multivariate regression analysis

$$\bar{f}_{cp} \approx \sum_{i=1}^{6} \beta_i \times \widetilde{CCF_i} \quad \text{with} \quad \widetilde{CCF_i} := \frac{CCF_i - \overline{CCF_i}}{\sigma(CCF_i)} \tag{1}$$

where $\bar{f}_{cp}$ is a vector where each elements stands for the average cold-pool fraction over the last 2 days of each simulation member of the ensemble when both precipitation and cold pools are present. Likewise, each CCF_i in the regression is a vector in which each element is the associated CCF_i of a simulation member of the ensemble. All the CCFs displayed in Table 1 are used as regressors. Regressors are standardized by subtracting their mean $\overline{CCF_i}$ and through dividing by their standard deviation $\sigma(CCF_i)$ across the entire ensemble. Therefore, β coefficients measure the relative significance of the CCFs with respect to each other with an equal weighting. Simulations without cold pools, that is, $\bar{f}_{cp} < 0.001$, are excluded. Out of the 87 *Botany* simulations that develop into clouds, this selection criterion yields 82 simulations. In addition, we removed simulations 7 and 39 from the regression analysis as they do not fully contain the second day due to technical issues (Jansson et al., 2023). Therefore, our multiple regression analysis (Equation 1) contains the target values and regressors, which are vectors (or 1D arrays) of size 80 × 1.
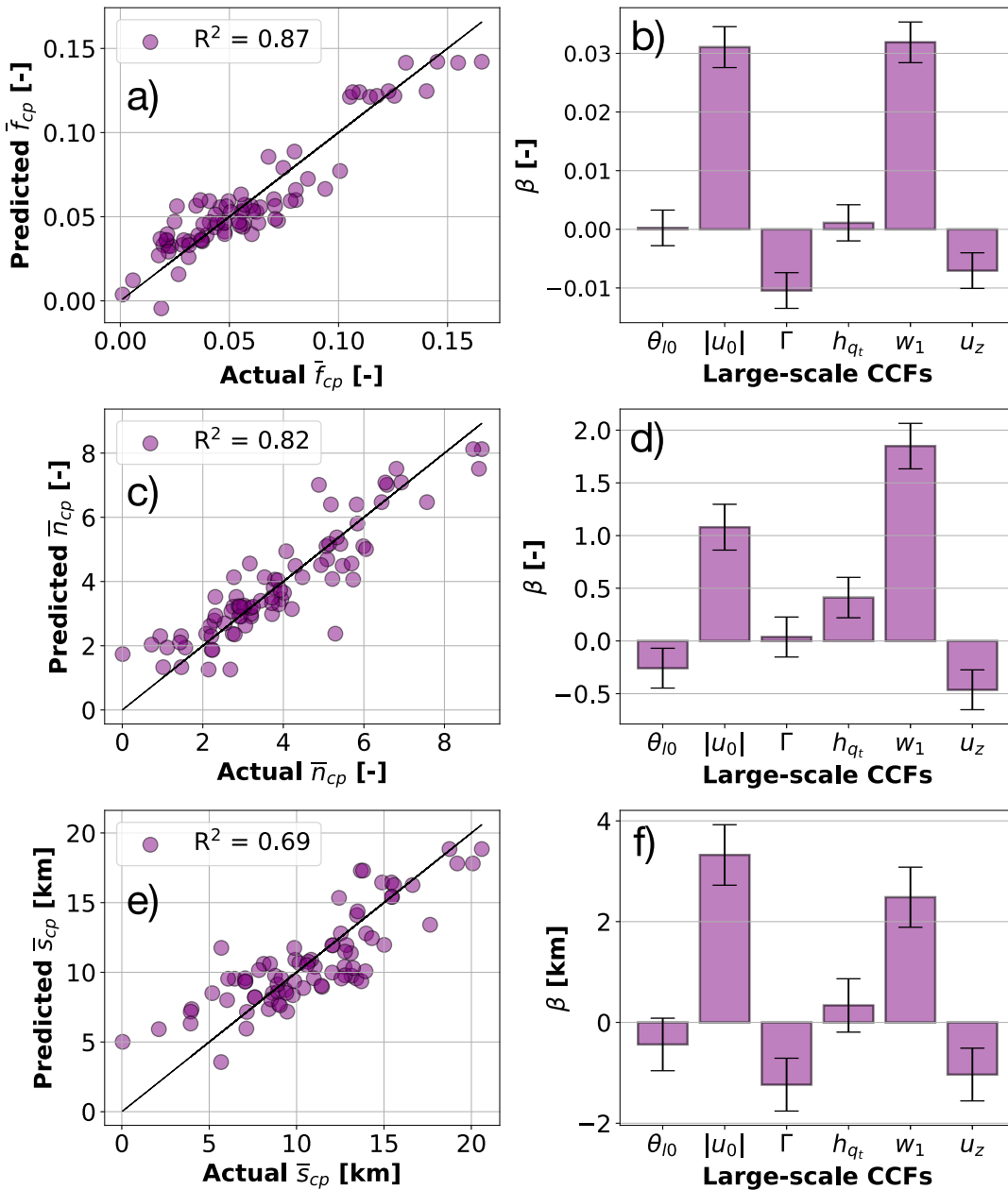
Figure 4. Multivariate regression of CCFs to predict cold-pool statistics. (a, c, e) The scatter plot of the results of multivariate regression analysis for $\bar{f}_{cp}$, $\bar{n}_{cp}$, and $\bar{s}_{cp}$ over the last 2 days of the *Botany* ensemble, where each purple circle stands for one simulation and the black line represents $y = x$. (b, d, f) The standardized beta coefficients (β) of the multiple regression analysis for predicting $\bar{f}_{cp}$, $\bar{n}_{cp}$, and $\bar{s}_{cp}$ as a function of *Botany*'s CCFs. Black error bars indicate the 95% confidence interval of each CCF. The greater the distance of the error bar from zero, the more significant the associated CCF in the regression model (smaller *p*-values). The *p*-values of the *F*-statistic test for all regression models are smaller than 10^{-17}.

Figure 4a shows that the regression model based on *Botany*'s CCFs is well capable of explaining the variations of the mean cold pool fraction $\bar{f}_{cp}$ between the different simulations with $R^2 = 0.87$. More specifically, Figure 4b shows that the near-surface geostrophic wind speed and large-scale subsidence are the most important CCFs for explaining the variability of cold pools in the entire ensemble: Cold pools are favored by stronger $|u_0|$ and weaker cloud-layer subsidence (stronger w_1 corresponds to weaker subsidence (Jansson et al., 2023)). Weaker but still significant correlations are observed for Γ and u_z: stronger free-tropospheric stability and horizontal (backward) wind shear lead to a smaller $\bar{f}_{cp}$.

The cold pool fraction f_{cp} depends on both the number and size of cold-pool objects within each cloud field. Therefore, we also conduct the same regression analysis on $\bar{n}_{cp}$, the mean number of cold pools, and $\bar{s}_{cp}$, the mean size of cold pools. Figures 4c and 4e show that the CCFs are also well capable of explaining the variations of $\bar{n}_{cp}$ and $\bar{s}_{cp}$ with R^2 values of 0.82 and 0.69, respectively. Also here both wind speed u_0 and subsidence w_1 emerge as the most significant CCFs for explaining the variability of $\bar{n}_{cp}$ and $\bar{s}_{cp}$, consistent with the results of $\bar{f}_{cp}$ (Figures 4d and 4f). Furthermore, the influence of Γ on $\bar{f}_{cp}$ appears to be primarily driven by the response of $\bar{s}_{cp}$ to Γ, as $\bar{n}_{cp}$ does not exhibit any significant response to Γ (Figures 4d and 4f). The response of our simulated cold pools to θ_{l0} and h_{q_t} seems to not be significant. In addition, we test the extent to which our results are sensitive to the definition of cold pools: the same multivariate regression based on cold pools being defined as where $h_{mix} < 400$ m ends up in almost identical results (Figure S1 in Supporting Information S1).

What are the underlying mechanisms through which cold pools respond to wind speed $|u_0|$, large-scale subsidence w_1, and stability Γ? In small-domain LESs of non-precipitating cumulus fields, Nuijens and Stevens (2012) showed that increased wind speed $|u_0|$ leads to stronger surface latent and sensible heat fluxes promoting deeper and more active cumulus convection. The deepening response to increased wind speed $|u_0|$ is also consistent with observations of the trades (Nuijens et al., 2009). Despite a modest response of the boundary-layer depth to wind speed $|u_0|$ perturbations in small-domain LESs of precipitating cases (Bretherton et al., 2013), similar regression analyses as Equation 1 show that, in the *Botany* ensemble, increased wind speed $|u_0|$ leads to deeper cloud fields that contain larger amount of liquid water (Figures S2 and S3 in Supporting Information S1).

Weaker subsidence (larger w_1) reduces both the large-scale heating and drying of the cloud layer, allowing deeper cloud layers, consistent with observations (Nuijens et al., 2009). Likewise, increased stability prevents the deepening of the boundary layer, thereby limiting the growth of cloud fields' depth (Bellon & Stevens, 2012, Figure 3). These responses are also consistent in the *Botany* data set: regression analyses of the entire ensemble show that both cloud-top height and liquid-water path increase in response to decreased subsidence and stability (Figures S2 and S3 in Supporting Information S1).

Deeper trade cumuli with larger liquid-water paths eventually generate more intense precipitation, also in observations (e.g., Nuijens et al., 2009). Observational studies in the trades further showed that larger cold pools are associated with more vigorous precipitation-driven downdrafts (Vogel et al., 2021; Zuidema et al., 2012). Therefore, our *Botany*-based results mirror observations: deepening of the boundary-layer cloudiness leads to larger cold pools.

Most of the results of the regression analyses are also consistent with observations of mesoscale cloud patterns in the trades: the so-called *Gravel* and *Flower* patterns are strongly favored by windy environments (Bony et al., 2020; Schulz et al., 2021). These distinct patterns are also reported to consist of a large number of cold pools (Vogel et al., 2021). However, *Gravel* and *Flowers* patterns are associated with larger subsidence (Schulz et al., 2021), which contradicts our LES-based results. *Fish* patterns were not simulated (Jansson et al., 2023) as these mesoscale structures are too large (> 1,000 km) to be captured in the simulation domains of the *Botany* simulations and stem from extra-tropical cold fronts that intrude into the trades (Schulz et al., 2021).

Therefore, theory, models, and observations, where available, confirm (i) the deepening of cloud fields in response to increased wind speed, decreased free-tropospheric stability, and decreased large-scale subsidence, and (ii) the increasing size of cold pools in response to this deepening.

3.2. The Dependence of Cold-Pool Evolution on the Diurnal Cycle

Here, we investigate how the evolution of cold pools is modulated by the diurnal cycle (Figure 1, link 2). Figure 5a shows the time series of the average cold-pool fraction of the entire *Botany* ensemble. As expected from the time series of clouds and rain (Figure 2a), the dependence of cold pools on the diurnal cycle is clearly visible: there is a significantly larger cold-pool fraction during sunrise in comparison with sunset. This diurnality is due to the stronger radiative cooling during the nighttime that destabilizes the atmosphere, promoting stronger convection, more rain, and thereby more and larger cold pools. Despite the absence of diurnality in CCFs (e.g., subsidence, wind, sea-surface temperature) of the *Botany* simulations, it is noteworthy that these simulations featuring only diurnality in insolation can reproduce comparable evolution and range of variability in f_{cp} as reported in observations of the trades by Vogel et al. (2021).
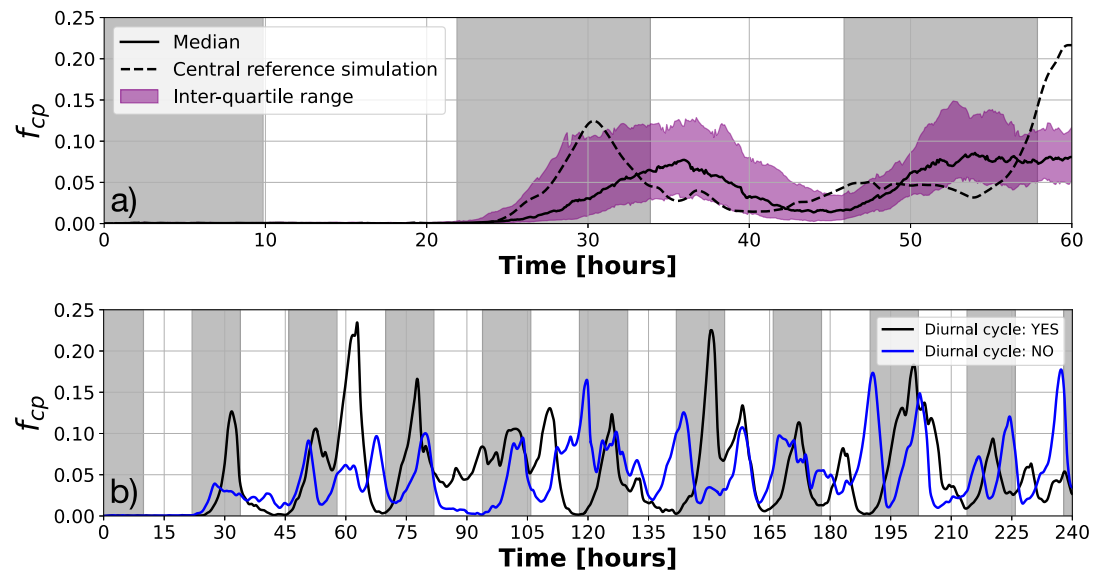
Figure 5. Effect of the diurnal cycle on cold pools. (a) The time series of the median f_{cp} (continuous line) accompanied by the interquartile range between the 25th and 75th percentiles of f_{cp} (purple shade) for the entire *Botany* ensemble. The f_{cp} time series of the central reference simulation is shown by the dashed line. (b) Time series of f_{cp} for the central reference simulation in the *Botany* data set with (black) and without (blue) the diurnal cycle. Gray-shaded areas correspond to nighttime.

To distinguish the cold-pool development forced by the daily cycle from any development due to pure self-organization, we select the central reference simulation (i.e., run 1 of the ensemble) which has the mean CCFs of the *Botany* hypercube, and conduct a simulation without diurnality in incoming solar radiation. To achieve this, we calculate the average solar radiation over 24 hr and determine the corresponding solar zenith angle. We then run DALES, keeping the zenith angle fixed at the calculated value (similar to Ruppert and Johnson (2016)), resulting in a simulation with the same total incoming solar radiation each day. This simulation is run over 10 days, and its results are plotted in Figure 5b.

Figure 5b still shows an intermittent behavior in the time series of f_{cp}, even when the diurnality in insolation is absent. The fluctuations in fraction (Figure 5b), number, and size (Figure S4 in Supporting Information S1) of cold pools in the simulation without the diurnal cycle exhibit higher frequency but mostly with smaller amplitudes. The latter is due to the time-invariant shortwave radiative heating, constantly stabilizing the atmosphere, preventing clouds from getting as deep as nighttime, reducing the amplitude of cold-pool fluctuations. This is supported by the nighttime peaks in f_{cp}, which are about twice as large in the simulation with the diurnal cycle compared to the one without (Figure 5b). This led us to ask: Why does the intermittent behavior persist even in the simulation without the diurnal forcing? Answering this question sheds light on the dependence of cold pools on self-organizing mechanisms (Figure 1, link 3).

3.3. The Dependence of Cold Pools on Self-Organizing Mechanisms

As cold pools are the direct result of rain-evaporation-driven downdrafts, it is natural to expect a similar temporal behavior of precipitation and other cloud properties that promote rain formation. Indeed, Figure 6a shows that cloud fraction f_c, liquid-water path $\mathcal{L}$, and surface precipitation rate $\mathcal{P}$ (the latter two both conditioned on cloudy columns) display a very similar intermittent behavior as the cold-pool fraction f_{cp}. This is further supported by Figure 6b which shows strong correlations of the cloud field properties f_c, $\mathcal{L}$, and $\mathcal{P}$ with f_{cp} with lags of 0.5, 2.7, and 2.4 hr, respectively. These lag-correlations support the familiar sequence of events leading to cold pools: clouds grow deeper, increase their liquid-water content that promotes precipitation, leading to the formation of cold pools. The question now is what role cold pools play in driving this evolution.

Studies in deep convection (e.g., Haerter et al., 2019; Nissen & Haerter, 2021) showed that the interaction between cold pools through their collisions is an essential mechanism for the self-organization of deep convective cloud fields. Here, in our idealized simulation of trade cumulus, we hardly observe such interactions as the
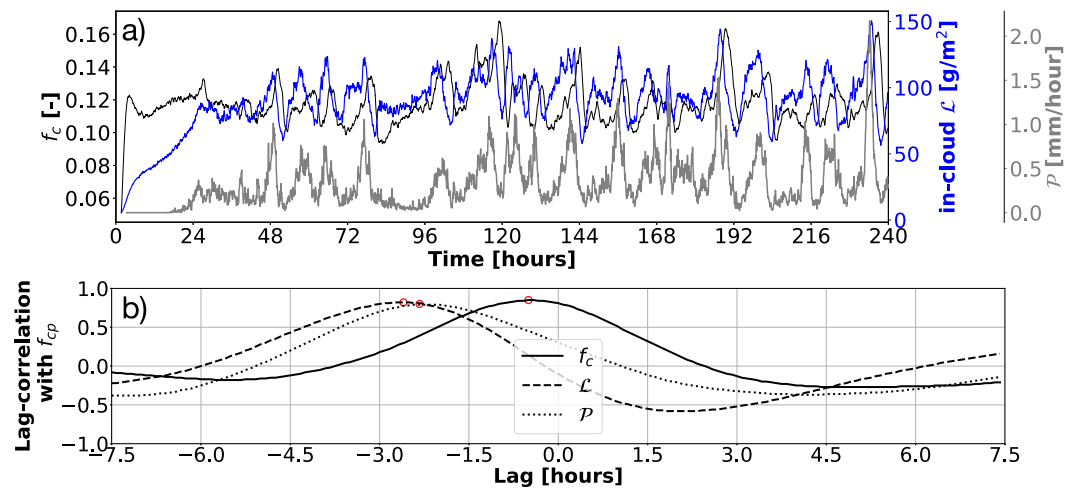
Figure 6. Cloud-rain-cold-pool correlations. (a) Time series of f_c, $\mathcal{L}$, and $\mathcal{P}$. (b) Lag-correlations of f_{cp} with f_c (continuous line), the in-cloud $\mathcal{L}$ (dashed line), and the in-rain $\mathcal{P}$ (dotted line). The highest correlations are marked by the red circle. The correlations are based on the last 5 days of the simulation without the diurnal cycle, during which the domain-mean total-water path has stabilized (Figure S5 in Supporting Information S1).

number and fraction of cold pools are too small for frequent collisions (Figure 5b; Figure S4 in Supporting Information S1, Movie S1). We speculate that this might be due to the structure of shallow mesoscale overturning circulations. Once these circulations aggregate cloud fields, their descending branches tend to separate the aggregated clouds from each other. Consequently, subsequent cold pools form far apart, preventing them from interacting with each other through collisions. This brings us to ask: what self-reinforcing feedback does govern the observed intermittent behavior (Figure 1, link 3)?

To answer this question, we suggest a mechanism through which cold pools play a role in the self-organization of the trade-cumulus cloud fields. Firstly, we begin by qualitatively describing these mechanisms using snapshots that depict the stages of a typical cold pool and its parent cloud's life cycle, referred to hereafter as the "cold-pool system" (Section 3.3.1). We show these snapshots which, through visual inspection, are representative of nearly all cold pools forming in our simulation (Movie S1). Secondly, we offer statistical support for the explained mechanisms throughout the simulation (Section 3.3.2). Finally, we close this section by summarizing and discussing the points that are necessary to be considered in future research (Section 3.3.3).

3.3.1. Three Stages of Self-Organization of the Cold-Pool Systems

Figure 7 shows the stages of the cold-pool system's life cycle, where we track one cold-pool system over hours 164–167 from both top and side views. This life cycle of the cold-pool system suggests a clear physical mechanism that governs the growth and decay of cold pools. Throughout the explanation of the life-cycle stages of cold pools below, we refer to the processes by numbers that are also shown in Figure 7.

Developing stage. *Hour 164*. During this developing stage, the cold-pool system (at $y \approx 80 - 90$ km) is relatively small in the horizontal (y direction) and displays self-reinforcing dynamics: precipitating downdrafts on the Southern part of the cold-pool system (1) suppress the mixed-layer height and induce a strong Northern outflow toward the boundary of the cold pool (2). Directly outside the cold pool, where the mixed layer still has a top close to the lifting condensation level (LCL), strong convergence of the outflow induces updrafts and the formation of active cumulus convection (3). These growing cumulus clouds appear to be pushed back into the cold-pool region by a strong convergence at the cloud base of the actively precipitating part of the system (4), where they reinforce the downdrafts through the precipitation that they produce. Finally, around the inversion at a height of 3 km, a region of strong divergence (an anvil outflow) can be observed (5).

Mature stage. *Hour 165*. At this stage, the cloud system has extended horizontally with the anvil outflow, partially covering the cold pool at $y \approx 79 - 95$ km (5). Underneath this outflow, a larger but also weaker precipitation band develops between $y \approx 80 - 90$ km, resulting in weaker downdrafts (1), a weaker surface outflow (2), and hence also a weaker gust front with less vigorous updrafts into shallower cumulus clouds aloft (3). Yet, the
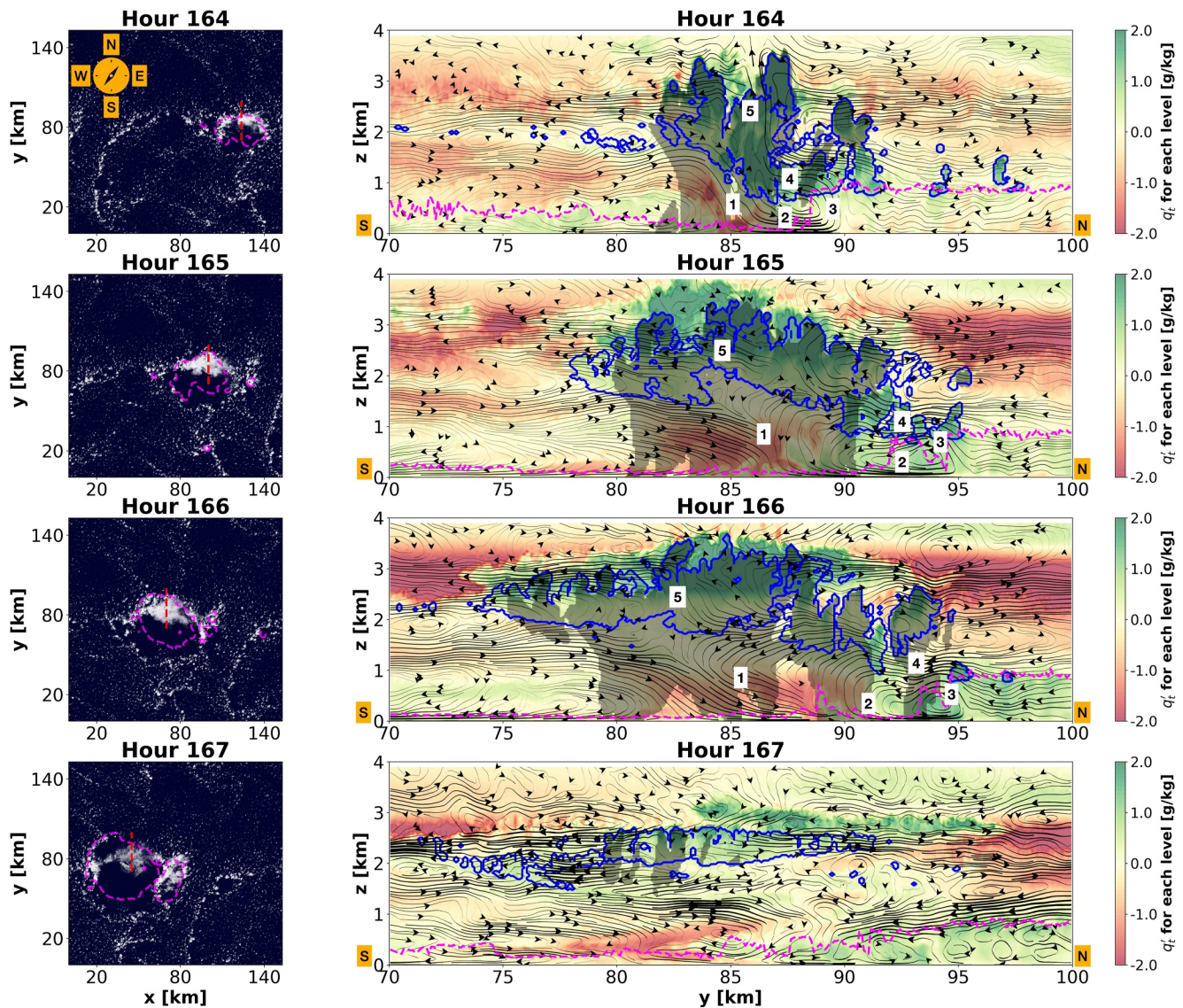
Figure 7. Typical stages of the cold-pool system's life cycle. The left column shows four contour plots of cloud albedo along with the cold-pool mask shown by the dashed, magenta contour lines for hours 164–167 of the simulation without the diurnal cycle. The right column shows y-z-cross-section contour plots of the total specific humidity anomalies associated with the dashed red line in snapshots shown in the left column. Cloud and rain boundaries are shown by the blue and gray contour lines. Circulations are made from the meridional (v) and vertical (w) velocity anomalies and are shown by black streamlines. To reduce the noise from the circulations, v, w are made from the medians of a 5-km window along the x dimension. The h_{mix} is shown by the dashed, magenta contour lines. The South (S), North (N), West (W), and East (E) directions are shown by orange labels.

connection with the cloudy updrafts at the gust front is still intact (4), such that the feedback from the developing stage remains sufficiently strong to sustain the system.

Decaying stage. *Hours 166, 167*. In the decaying stage (hour 166), the cloud extends further in the horizontal (5), mainly in the form of stratiform anvils. This leads to geometrically thinner clouds, which in turn contain less liquid water per cloudy column. Hence, the precipitation intensity reduces further (1), as do the diverging surface current (2) and the gust front (3), so that hardly any cumulus convection is formed on top of the updrafts (4). As a result, the moisture supply through the updrafts into the trailing anvils dwindles. The cold-pool system has now entered the decaying stage, after which at hour 167, the cloud object becomes thinner and vanishes quickly, leading to the presence of large clear-sky areas inside the cold-pool boundary (x-y cross-section).

3.3.2. Composite Analysis of Self-Organization of the Cold-Pool System

To provide statistical support for the processes described above, we investigate the evolution of the most important parameters of all cold-pool systems that develop over the last 5 days of the simulation without the diurnal cycle. For clouds, we use the domain-mean liquid-water path $\mathcal{L}$ and cloud thickness h (both averaged over cloudy columns), and the average size of cloud objects L_c in the simulation domain. For precipitation, we use the in-rain domain-mean precipitation intensity $\mathcal{P}$ and the domain-mean size of precipitation cells L_p. For cold pools, we use the maximum near-surface horizontal velocity inside cold pools $u_{cp,\max}$ to indicate the strength with which the cold pools diverge near the surface (see Figure S6 in Supporting Information S1). In addition, we use $w_{P_{99.99}}$, the 99.99$^{\text{th}}$ percentile of the vertical velocity (at 200-m height) as an indication of the convergence strength at the gust front near the boundary of cold pools. We use this percentile because the width of the convergence area at the gust front is narrow, but features vigorous updrafts (see Figure S6 in Supporting Information S1).

To highlight the evolution of the cold-pool system, we make a composite plot of the time series of all metrics mentioned above, that is, $\mathcal{L}$, h, $u_{cp,\max}$, $w_{P_{99.99}}$, L_c, and L_p during the last 5 days of the simulation without the diurnal cycle. To do so, we first find the corresponding time steps of the local minima of $\mathcal{P}$ time series. We find these local minima from the smoothed precipitation time series to avoid erroneously identifying very small noises as cold-pool events. As a result, for each cold-pool event i, we have a starting point t_i which is when precipitation starts, and an ending point t_{i+1} which is when precipitation stops. For each event i, we define a new time index

$$t^* = \frac{t - t_i}{t_{i+1} - t_i} \text{ where } t_i < t < t_{i+1}, \tag{2}$$

that ranges between 0 and 1. Since the length of cold-pool events may vary slightly throughout the simulation without a diurnal cycle, we linearly interpolate the time series of each event to ensure all cold-pool events have the same number of data points. Next, at each time step j in t^* for each cold-pool event i, we find the corresponding value C_{ij} of the metric $C \in \{\mathcal{L}, h, u_{cp,\max}, w_{P_{99.99}}, L_c, L_p\}$ and calculate the mean of it for all cold-pool events by

$$\overline{C}_j = \frac{\sum_{i=1}^{N} C_{ij}}{N}, \tag{3}$$

where N is the total number of cold-pool events. We normalize the composited evolution of each metric $\overline{C}$ by their minimum and maximum as

$$\overline{C}_{j,\text{normalized}} = \frac{\overline{C}_j - \min(\overline{C})}{\max(\overline{C}) - \min(\overline{C})}. \tag{4}$$

Figures 8a–8c show the final normalized composited time series $\left(\overline{C}_{\text{normalized}}\right)$. Figures 8a–8c show that $\mathcal{P}$ features an almost symmetric evolution: it robustly increases during $0 < t^* < 0.45$, stabilizes during $0.45 < t^* < 0.65$, and robustly decreases during $0.65 < t^* < 1$. These time blocks respectively mark each stage of the life cycle of the cold-pool system described and visualized in Section 3.3.1, that is, *Developing*, *Mature*, and *Decaying*.

Figure 8a illustrates that at the beginning of the *Developing* stage ($t^* = 0$), clouds are already deep enough to start raining, which aligns with Figure 6b. During this stage, Figure 8b shows that as precipitation intensity $\mathcal{P}$ increases, the strength of the near-surface diverging outflows $u_{cp,\max}$ and convergence at the cold-pool boundaries $w_{P_{99.99}}$ consistently increase. Simultaneously, clouds thicken, contain more liquid water (Figure 8a), and the overall size of clouds and precipitation cells robustly increase (Figure 8c). The growth of clouds both horizontally and vertically (Figures 7, 4,5), along with the increased precipitation downdrafts (Figures 7, 1), diverging outflows (Figures 7, 2), and converging updrafts (Figures 7, 3), are consistent with Figure 7 (from hour 164) and imply the presence of circulations through which cold pools feed back to the parent clouds.

During the *Mature* stage, Figure 8b shows that the time series of precipitation intensity $\mathcal{P}$, diverging outflows $u_{cp,\max}$ and converging updrafts $w_{P_{99.99}}$ are quite stable. Figures 8a and 8c indicate that while clouds begin to shrink vertically ($t^* \approx 0.55$), as shown by a decrease in $\mathcal{L}$ and h, they expand horizontally, as shown by an increase in L_c. This is an indication of the formation of stratiform anvils that are vertically thin but horizontally large. Figure 8c
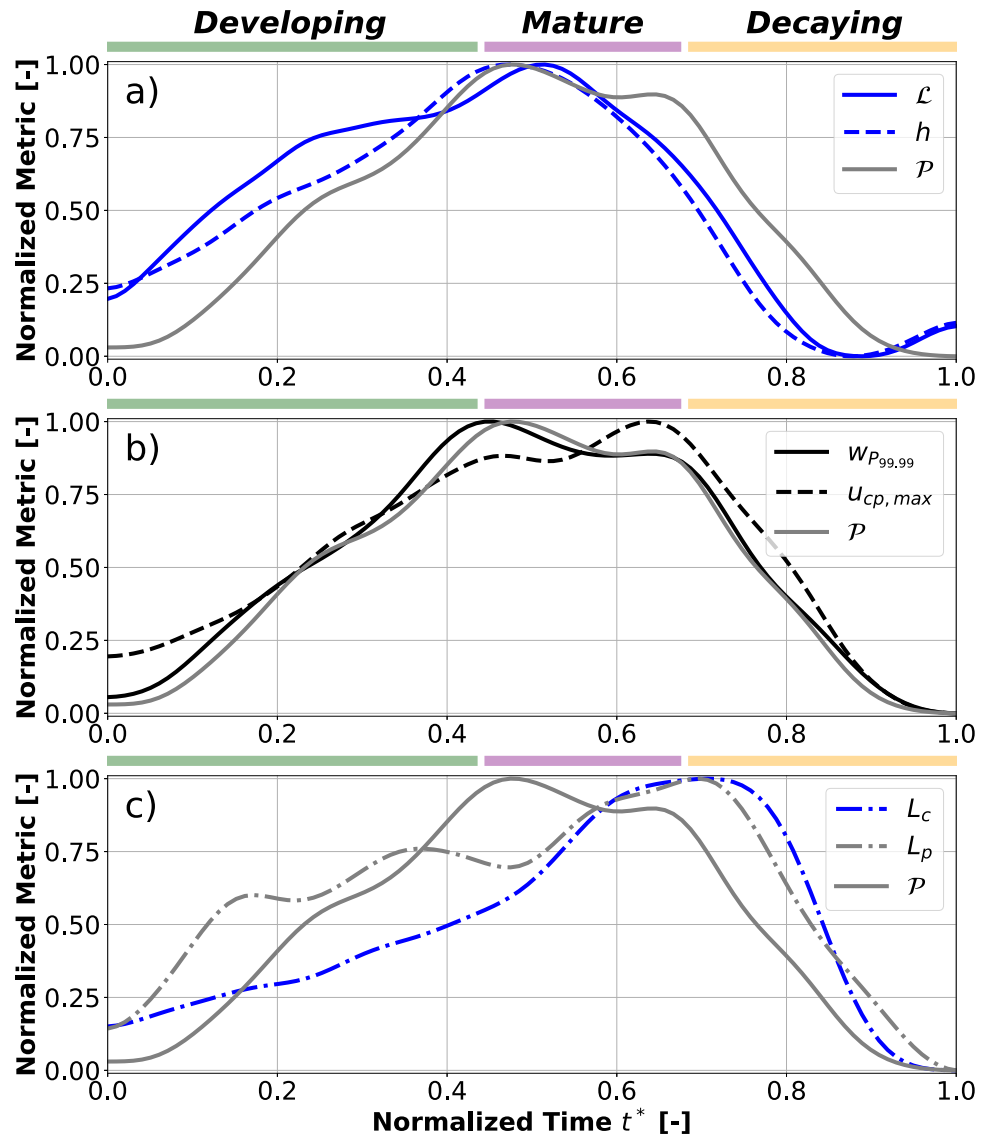
Figure 8. Composite analysis of the evolution of the cold-pool system. Composite time series of the evolution of the domain-mean precipitation intensity $\mathcal{P}$ with (a) the domain-mean liquid-water path $\mathcal{L}$ and cloud geometric thickness h, (b) maximum near-surface horizontal velocity at cold-pool areas $u_{cp,max}$ and the 99.99th percentile of vertical velocity $w_{P_{99.99}}$ at 200-m level, (c) domain-mean size of cloud objects L_c and precipitation cells L_p within the simulation domain for all life cycles of the cold-pool systems of the last five days of the simulation without the diurnal cycle. The stages of the cold-pool system *Developing*, *Mature*, *and Decaying* are marked by colors green, purple, and yellow, respectively. Composited time series were slightly smoothed using a Gaussian low-pass filter.

further highlights that the size of precipitation cells L_p is also growing alongside the size of clouds. This means that the same amount of rain evaporation must be occurring over a larger region, which reduces the potential for the cold pool to drive the system. Formation of stratiform anvils during this *Mature* stage is consistent with the development of the cold-pool system shown in Figure 7: from hour 164 to hr 165, both the width of the cloud and rain cells increase, while the average vertical thickness of the cloud decreases (Figures 7, 5).

Time series in Figures 8a–8c show that once clouds and precipitation cells reach their maximum size, the starting time of the *Decaying* stage is set; that is, once stratiform anvils form, they lead to precipitation with larger cells L_p but weaker intensity $\mathcal{P}$, consistent with Figure 7(1, during hours 164–166). As a result, Figure 8b shows that the near-surface diverging outflows at cold pools $u_{cp,max}$ (Figures 7, 2) and the convergence at the cold-pool fronts

$w_{P_{99,99}}$ (Figure 7, 3) get robustly weaker during the *Decaying* stage, such that they can hardly trigger formation of new clouds at LCL (Figures 7, 4, hour 166), consistent with what Figure 7(hour 166) illustrates. Note that during the *Decaying* stage, the size of both clouds L_c and precipitation cells L_p drop quite fast (Figure 8c) once $w_{P_{99,99}}$ reduces sufficiently, implying the quick disappearance of stratiform anvils after they detach from their convergence roots, as shown in Figure 7(hour 167).

3.3.3. Discussion and Outlook

In essence, the preceding analysis suggests that the role cold pools play in the trade-cumulus self-organization is through what we will call "shallow squall-line" dynamics. Thinking of the trade-cumulus cold-pool systems as squall lines has precedence in the analysis of mesoscale cloud rings without stratiform tops, visible in the so-called *Gravel* fields (Li et al., 2014). Yet, our findings suggest that the dynamics on a single cold pool edge also underlie the formation of the large anvils frequently found atop more clustered cloud systems. This resonates with the findings of Dauhut et al. (2023), who illustrated similar processes, though for a single case study, as in Figure 7 and proposed that the so-called *Flowers* are shallow mesoscale convective systems. In fact, our results indicate that most cold-pool systems in the trades develop through similar shallow squall-line dynamics, with only some growing as large as the case on 2 February 2020 (e.g., Narenpitak et al., 2021), and only some developing anvil clouds.

The difference between patterns with and without anvils might be related to inversion strength. In fields of *Flowers*, the inversion is strong (Bony et al., 2020, their Figure 2), such that strong cold-pool-induced convection leads to large stratiform outflows when they impinge on the inversion. Another possibility is that the cloud-to-rain droplet auto-conversion is less efficient in *Flower* patterns, as shown by Radtke et al. (2023). For the same amount of cloud water content, this gives *Gravel* fields a larger number of precipitation cells compared to *Flowers*. In turn, *Gravel* features a larger number of cold pools (Vogel et al., 2021, their Figure 7a), which gives room for cold pools to collide with each other, triggering the formation of new clouds at their collision point (Nissen & Haerter, 2021). In *Flowers*, and in our simulation ensemble, such interactions are rare, as cold pools frequently form quite far from each other. Future studies might attempt to distinguish these regimes and mechanisms in more detail, including how microphysical properties affect cold pools and their interactions with clouds.

We hypothesize that the updrafts being sheared and pushed back to the parent clouds at the cloud-base height (orange arrow in Figure 11) is due to a pressure gradient from the cold-pool front, where high pressure is induced by mechanically driven updrafts, to the inside of cold pools, where evaporative downdrafts lead to lower pressures. This causes the updraft to deflect toward the cold-pool area at the cloud base. The sheared updrafts at the boundary of our shallow squall lines resemble those in deep mesoscale convective systems (Rotunno et al., 1988; Stensrud et al., 2005; Weisman & Rotunno, 2004). These cold-pool-induced circulations can reinforce their parent clouds if their induced wind shear is twice that of the ambient environment (Li et al., 2014, their Figure 15c). In addition, according to Li et al. (2014), we expect a "downwind triggering," given our zonal wind is westward and features forward shear in the sub-cloud layer, resulting from the interplay between ambient environmental shear and cold-pool-induced shear. Although our simulations feature zero meridional geostrophic wind (south-north direction), we consistently observe triggering on the northern side of cold pools. Hence, further investigating the interaction between cold-pool-induced and environmental shear might help understand the causality of this cloud-cold-pool coupling, which we defer to future studies.

3.4. Implications for Mesoscale Cloud Organization and Radiative Effect

Considering our conceptual picture (Figure 1), we have shown how cold pools respond to CCFs (Figure 1, link 1; Section 3.1) and the diurnal cycle of radiation (Figure 1, link 2; Section 3.2). Keeping these CCFs time-invariant, we suggested that the cold pools organize trade-cumulus fields through shallow squall-line dynamics, which drives the self organization of cold-pool systems (Figure 1, link 3; Section 3.3). Here, we want to understand (i) how these self-organizing mechanisms manifest themselves as 2D cloud patterns (Section 3.4.1), and (ii) whether and how they matter for trade-cumulus radiative effect (Figure 1, link 4; Section 3.4.2).

3.4.1. Dependence of Mesoscale Organization on Cold Pools

To investigate the spatial organization of cloud fields throughout the cold-pool systems' life cycles, we use the average cloud size L_c and calculate the open-sky fraction L_o, the mean fraction of cloud-free areas in the
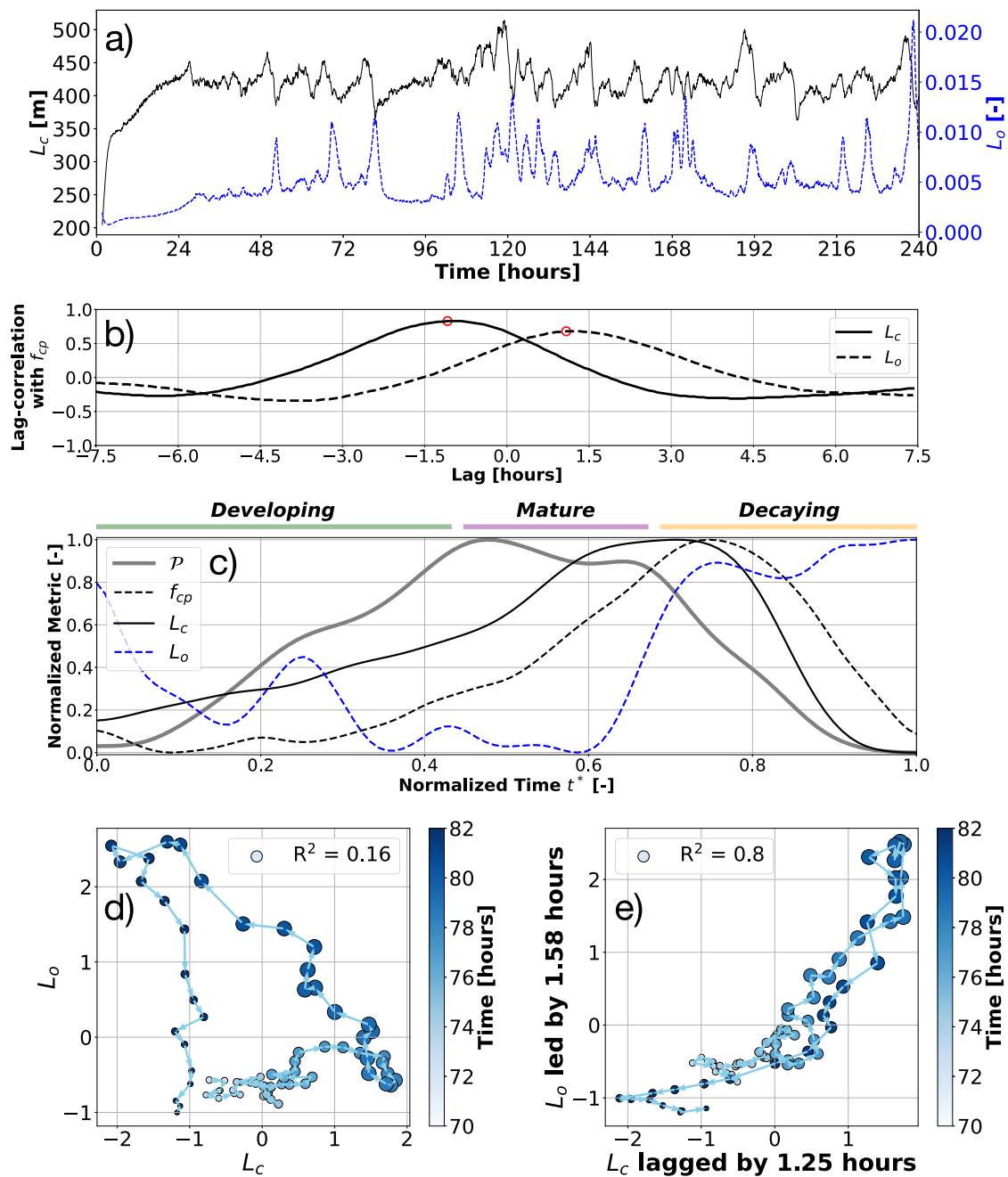
Figure 9. Cold-pool-mesoscale organization relationships. (a) Time series of L_c and L_o. (b) Lag-correlations of f_{cp} with L_c and L_o, with red circles showing the best correlations. (c) Similar composite analysis to Figure 8 for $\mathcal{P}, f_{cp}, L_c$, and L_o of the simulation without the diurnal cycle. (d) The evolution of the standardized L_c and L_o (concerning their mean and standard deviations) through one cold pool's life cycle (hours 70–82). (e) The same relationship as (d) but with lags with respect to f_{cp} time series. The size of each circle in both plots is scaled by the value of f_{cp} at the corresponding time step. The correlations are based on the last 5 days of the simulation without the diurnal cycle.

simulation domain. These metrics effectively capture the mesoscale organization variability, in observations (Janssens et al., 2021) and in the *Botany* ensemble (Janssens, 2023, chapter 7). Figure 9a shows the time series of these metrics over the 10-day period of the central reference simulation without the diurnal cycle: L_c grows fast during the first 24 hr of the simulation, when clouds are non-precipitating. This marks phase 1 from Figure 1, where convergent moist areas with non-precipitating cumulus convection and divergent dry areas with less cumuli grow together. This phase is broken by rain and cold-pool formation around hour 24, after which the cloud

scale L_c does not grow anymore but shows an intermittent behavior, comparable to the cold-pool fraction f_{cp} (Figure 1, Option iii). This intermittency is also present in the time series of the open-sky fraction L_o. Figure 9b shows that L_c has a maximum correlation with f_{cp} with a lag of ≈ -1 hr, while L_o has its maximum correlation with a lag of $\approx +1$ hr, consistent with the cold-pool systems' life cycle (Figures 7 and 8): during both the *Developing* and *Mature* stages, the size of clouds L_c and cold pools f_{cp} grow until stratiform anvils form, which marks the beginning of the *Decaying* stage, during which the remaining anvils shrink in size, after which cold pools start to dwindle, raising the open-sky fraction L_o (Figure 9c).

According to Janssens et al. (2021, their Figure 3a); Janssens et al. (2023, their Figure 7.1a), L_c and L_o provide complementary information about shallow cumulus organization and, in combination, can explain most of the variability in organization observed in the trades. Figure 9d shows how the $L_c - L_o$ relationship evolves throughout one cold-pool cycle. Interestingly, our cross-correlation analysis in Figures 9b and 9e shows that L_c and L_o are tightly lag-correlated, even though they are independent. This suggests that precipitating trade-cumulus organization can be captured by two dimensions: (i) one spatial organization or process-related metric, which can be one of $f_c, \mathcal{L}, h, \mathcal{P}, f_{cp}, L_c$, and L_o and (ii) one temporal organization metric, which measures the lag between, for instance, L_c and L_o; or equivalently how fast the first dimension evolves through one cold-pool system's life cycle.

3.4.2. Dependence of Cloud-Radiative Effect on Cold Pools

Mesoscale organization affects the trade-cumulus radiative effect through variations in cloud cover f_c (Bony et al., 2020) and optical thickness τ_c (Alinaghi et al., 2024; Denby, 2023). So, since cold pools affect cloud organization (Figure 9), we expect cold pools to affect CRE. To investigate this, we perform the same composite analysis of Section 3.3.2 and Figure 8 for the domain-mean CRE, f_c, and $\mathcal{L}$. In the *Botany* simulations, the cloud-droplet number concentration is fixed, so the variations in τ_c are fully determined by the variations in $\mathcal{L}$.

As a result, Figure 10a highlights that during the *Developing* stage of the cold-pool systems, CRE gets stronger and reaches its maximum value once the system is in its *Mature* stage. During this stage when stratiform anvils are forming, f_c increases, while $\mathcal{L}$ decreases, which leads to CRE remaining stable at its maximum value. During the *Decaying* stage, cold-pool dynamics get weak and anvils vanish, leading to a decrease of f_c, $\mathcal{L}$, and therefore CRE. Our analysis demonstrates that cold pools influence CRE by modulating cloudiness both horizontally and vertically, as captured by f_c and $\mathcal{L}$. Furthermore, this analysis reveals that f_c and $\mathcal{L}$ evolve differently over the various stages of the cold pool system's life cycle. Therefore, to accurately assess the impact of cold pools on cloudiness, sampling at a single moment is insufficient. Instead, it is necessary to sample, for example, by averaging, over all stages of cold-pool systems' life cycle.

Averaging over the daily time scale, along with the influence of the diurnal cycle, may lead to more intricate cold-pool-CRE relationships. Specifically, cold-pool events occurring at night contribute to the daily mean cold-pool fraction but do not affect shortwave radiative effects, which, by definition, only occur during the daytime (Figure S7 in Supporting Information S1). This prompted us to ask the following questions: How frequently do cold pools occur during daytime? and, given the same daily mean cold-pool fraction, to what extent does the timing of cold pools influence their impact on CRE?

To answer these questions, we employ the data from the entire *Botany* ensemble and first introduce the metric $r_{cp,day}$

$$r_{cp,day} = \frac{\sum_{t=34}^{46} f_{cp,t}}{\sum_{t=22}^{46} f_{cp,t}} \tag{5}$$

where $\sum_{t=34}^{46} f_{cp,t}$ and $\sum_{t=22}^{46} f_{cp,t}$ are the sums of cold-pool fraction over the daytime (34–46 hr) and the entire second day (22–46 hr), respectively. Thus, $r_{cp,day}$ measures the daytime contribution of cold-pool events to the daily mean cold-pool fraction $\bar{f}_{cp}$ averaged over hours 22–46. Figure 10b shows $\bar{r}_{cp,day} \approx 0.5$. This is consistent with Figure 5a and with the fact that simulated cold pools tend to form during the night and peak slightly after sunrise. Figure 10b further illustrates that while simulations with large $\bar{f}_{cp}$ $(\bar{f}_{cp} > 0.1)$ feature similar $r_{cp,day}$ of around 0.4, there is significantly more variability in $r_{cp,day}$ $(\approx 0.2 - 1)$ for simulations with relatively small $\bar{f}_{cp}$
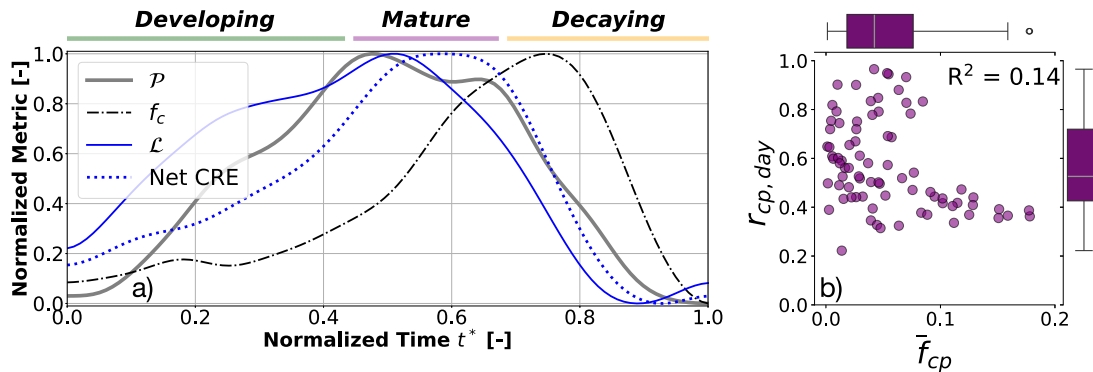
Figure 10. Dependence of cloud-radiative effect on cold pools. (a) Similar composite analysis to Figure 8 for $\mathcal{P}, f_c, \mathcal{L}$, and net CRE (shortwave SW + longwave LW) of the simulation without the diurnal cycle. (b) The 2D scatter plot of the daily mean cold-pool fraction $\overline{f}_{cp}$ and the fraction of daytime contribution to this mean $r_{cp,day}$ quantified by Equation 5 for the entire *Botany* ensemble.

$(0 < \overline{f}_{cp} < 0.1)$: across the entire ensemble, $r_{cp,day}$ and $\overline{f}_{cp}$ are not strongly correlated (see also Figure S8 in Supporting Information S1).

Therefore, both the factors that control the total cold-pool occurrence over a day $(\overline{f}_{cp})$ and those that control the relative distribution of f_{cp} between day and night $(r_{cp,day})$ have the potential to independently affect the CRE. Yet, we cannot quantify this effect here, for example, through multivariate regression across the entire *Botany* ensemble, because the imposed variability in large-scale CCFs across the ensemble control variability both in the cold pools (as shown in Section 3.1) and in the daily mean CRE (Janssens, 2023; Janssens et al., 2024). Therefore, the relationship between daily mean cold-pool fraction and CRE across *Botany* is significantly confounded by CCFs. For example, the strength of imposed near-surface geostrophic wind $|u_0|$ appears to strongly control both cold-pool fraction (Figure 4) and CRE (Janssens et al., 2024). Conversely, free-tropospheric humidity h_{q_t} relates strongly to CRE, but not to cold pools. Hence, to truly determine whether cold pools and their diurnal timing, independent of CCFs, affect the CRE, we are currently conducting a study to investigate how removing cold pools (Böing et al., 2012) affects CRE and its response to CCFs across the *Botany* ensemble.

4. Summary

Observed covariations between cold pools and mesoscale organization (Vogel et al., 2021) suggest a potential impact of cold pools on radiative effects of clouds forming in the trade-wind regime. This led us to start this paper by asking three questions: (i) to what extent are cold pools controlled by the large-scale cloud-controlling factors (CCFs) (Figure 1, link 1) and the diurnal cycle of insolation (Figure 1, link 2)?; (ii) through what underlying
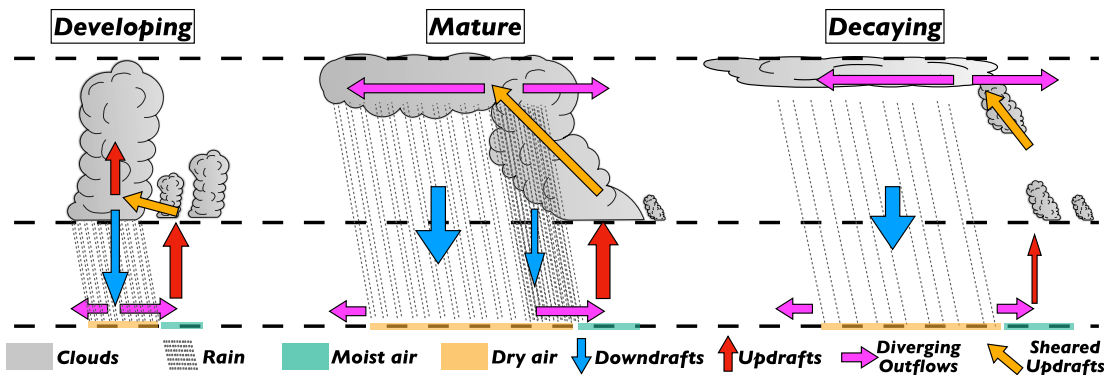

Figure 11. Conceptual schematic of the cold-pool system. Schematic of the cold-pool system evolution during the *Developing*, *Mature*, and *Decaying* stages as shown in Section 3.3 under Figures 7 and 8.

mechanisms do trade-cumulus cold pools evolve and interact with clouds (Figure 1, link 3)?; and (iii) what implications do these mechanisms have for mesoscale organization and cloud-radiative effect (Figure 1, link 4)?

To answer question (i), we employed an ensemble of high-resolution LES simulations, *Cloud Botany* (Jansson et al., 2023), and showed that cold pools are largely regulated by CCFs (Figure 4a). More specifically, cold pools are more frequent and larger in environments with stronger geostrophic wind speeds and weaker large-scale subsidence in the cloud layer (Figure 4b). In addition, cold-pool evolution is tightly synced with the diurnality in incoming solar radiation (Figure 5a).

To answer question (ii), we removed the diurnality in the insolation and found that cold pools show an intermittent behavior (Figures 5b and 6), which is driven by a complex interaction between clouds and cold pools. We find that this interaction expresses itself through shallow squall lines, whose evolution we summarize in the conceptual Figure 11. It is composed of precipitating downdrafts (blue arrows), near-surface diverging outflows (magenta arrows), and converging updrafts at cold-pool gust fronts (red arrows), which reinforce the parent clouds (Figures 7, 8, and 11, orange arrows). This shallow mesoscale convective system develops and reaches a mature phase until stratiform anvils form, leading to stratiform precipitation, weakening the downdrafts, diverging outflows, and converging cold-pool-induced updrafts (Figure 11, central panel), until they hardly trigger formation of new clouds, and the system decays (Figures 8 and 11, right panel).

Finally, to answer question (iii), we quantified that cold pools affect mesoscale cloud organization by modulating the length scale and the open-sky fraction (Figure 9). In the end, we showed that cold pools increase CRE once shallow squall lines are developing, until the point at which stratiform anvils form, when CRE stabilizes and reaches its maximum. Afterward, the stratiform precipitation and the resulting decay in squall lines lead to a decrease in CRE (Figure 10a).

Moreover, we showed that the CRE dependence on cold pools is more complex when the diurnal cycle is present: to affect CRE, cold-pool events must occur during the day (Figure 10b). This means that the synchronization of cold pools with the diurnal cycle of insolation affects the extent to which CRE is regulated by cold pools. Note that, unlike our idealized simulations, the diurnality in the trades is profound in the most important CCFs, that is, wind speed and stability (Vial et al., 2021). Given the strong dependence of cold pools on these CCFs (Figure 4), investigating (i) how fast mesoscale cold pools adjust to these CCFs, and (ii) how synchronous this adjustment is with the diurnal cycle of insolation might improve our understanding of the effect of mesoscales on trade-cumulus feedback.

Last but not least, despite the efforts made within this study, we still face the question of whether cold pools, as a self-organizing process at the mesoscales, affect cloudiness independently of large scales (Janssens, 2023; Janssens et al., 2024). We are currently working on addressing this question in our next study.

Data Availability Statement

The *Cloud Botany* data set is accessible through the EUREC⁴A intake catalog (https://howto.eurec4a.eu/botany_dales.html). The data is analyzed using Python (libraries: Numpy (Harris et al., 2020), Xarray (Hoyer & Joseph, 2017), Pandas (Wes McKinney, 2010), Scipy (Virtanen et al., 2020), Matplotlib (Hunter, 2007), Statsmodel (Seabold & Perktold, 2010), and Seaborn (Waskom, 2021)).

References

Alinaghi, P., Janssens, M., Choudhury, G., Goren, T., Siebesma, A. P., & Glassmeier, F. (2024). Shallow cumulus cloud fields are optically thicker when they are more clustered. *Quarterly Journal of the Royal Meteorological Society*, 150(763), 3566–3577. https://doi.org/10.1002/qj.4783

Anurose, T. J., Bašták Ďurán, I., Schmidli, J., & Seifert, A. (2020). Understanding the moisture variance in precipitating shallow cumulus convection. *Journal of Geophysical Research: Atmospheres*, 125(1), e2019JD031178. https://doi.org/10.1029/2019JD031178

Bellon, G., & Stevens, B. (2012). Using the sensitivity of large-eddy simulations to evaluate atmospheric boundary layer models. *Journal of the Atmospheric Sciences*, 69(5), 1582–1601. https://doi.org/10.1175/JAS-D-11-0160.1

Böing, S. J., Jonker, H. J., Siebesma, A. P., & Grabowski, W. W. (2012). Influence of the subcloud layer on the development of a deep convective ensemble. *Journal of the Atmospheric Sciences*, 69(9), 2682–2698. https://doi.org/10.1175/JAS-D-11-0317.1

Bony, S., Schulz, H., Vial, J., & Stevens, B. (2020). Sugar, gravel, fish, and flowers: Dependence of mesoscale patterns of trade-wind clouds on environmental conditions. *Geophysical Research Letters*, 47(7), e2019GL085988. https://doi.org/10.1029/2019GL085988

Bony, S., Stevens, B., Ament, F., Bigorre, S., Chazette, P., Crewell, S., et al. (2017). EUREC⁴A: A field campaign to elucidate the couplings between clouds, convection and circulation. *Surveys in Geophysics*, 38(6), 1529–1568. https://doi.org/10.1007/s10712-017-9428-0

Bretherton, C. S., & Blossey, P. (2017). Understanding mesoscale aggregation of shallow cumulus convection using large-eddy simulation. *Journal of Advances in Modeling Earth Systems*, 9(8), 2798–2821. https://doi.org/10.1002/2017MS000981

Bretherton, C. S., Blossey, P. N., & Jones, C. R. (2013). Mechanisms of marine low cloud sensitivity to idealized climate perturbations: A single-LES exploration extending the CGILS cases. *Journal of Advances in Modeling Earth Systems*, *5*(2), 316–337. https://doi.org/10.1002/jame.20019

Chen, Y.-S., Zhang, J., Hoffmann, F., Yamaguchi, T., Glassmeier, F., Zhou, X., & Feingold, G. (2024). Diurnal evolution of non-precipitating marine stratocumuli in an LES ensemble. *EGUsphere*, 1–42. https://doi.org/10.5194/egusphere-2024-1033

Dauhut, T., Couvreux, F., Bouniol, D., Beucher, F., Volkmer, L., Pörtge, V., et al. (2023). Flower trade-wind clouds are shallow mesoscale convective systems. *Quarterly Journal of the Royal Meteorological Society*, *149*(750), 325–347. https://doi.org/10.1002/qj.4409

Denby, L. (2023). Charting the realms of mesoscale cloud organisation using unsupervised learning. arXiv preprint arXiv:2309.08567. https://doi.org/10.48550/arXiv.2309.08567

Drager, A. J., & van den Heever, S. C. (2017). Characterizing convective cold pools. *Journal of Advances in Modeling Earth Systems*, *9*(2), 1091–1115. https://doi.org/10.1002/2016MS000788

Feingold, G., McComiskey, A., Yamaguchi, T., Johnson, J. S., Carslaw, K. S., & Schmidt, K. S. (2016). New approaches to quantifying aerosol influence on the cloud radiative effect. *Proceedings of the National Academy of Sciences of the United States of America*, *113*(21), 5812–5819. https://doi.org/10.1073/pnas.1514035112

Glassmeier, F., & Feingold, G. (2017). Network approach to patterns in stratocumulus clouds. *Proceedings of the National Academy of Sciences of the United States of America*, *114*(40), 10578–10583. https://doi.org/10.1073/pnas.1706495114

Glassmeier, F., Hoffmann, F., Johnson, J. S., Yamaguchi, T., Carslaw, K. S., & Feingold, G. (2019). An emulator approach to stratocumulus susceptibility. *Atmospheric Chemistry and Physics*, *19*(15), 10191–10203. https://doi.org/10.5194/acp-19-10191-2019

Gryspeerdt, E., Glassmeier, F., Feingold, G., Hoffmann, F., & Murray-Watson, R. J. (2022). Observing short-timescale cloud development to constrain aerosol–cloud interactions. *Atmospheric Chemistry and Physics*, *22*(17), 11727–11738. https://doi.org/10.5194/acp-22-11727-2022

Haerter, J. O., Böing, S. J., Henneberg, O., & Nissen, S. B. (2019). Circling in on convective organization. *Geophysical Research Letters*, *46*(12), 7024–7034. https://doi.org/10.1029/2019GL082092

Harris, C. R., Millman, K. J., van der Walt, S. J., Gommers, R., Virtanen, P., Cournapeau, D., et al. (2020). Array programming with NumPy. *Nature*, *585*(7825), 357–362. https://doi.org/10.1038/s41586-020-2649-2

Helfer, K. C., & Nuijens, L. (2021). The morphology of simulated trade-wind convection and cold pools under wind shear. *Journal of Geophysical Research: Atmospheres*, *126*(20), e2021JD035148. https://doi.org/10.1029/2021jd035148

Hersbach, H., Bell, B., Berrisford, P., Hirahara, S., Horányi, A., Muñoz-Sabater, J., et al. (2020). The ERA5 global reanalysis. *Quarterly Journal of the Royal Meteorological Society*, *146*(730), 1999–2049. https://doi.org/10.1002/qj.3803

Heus, T., van Heerwaarden, C. C., Jonker, H. J., Pier Siebesma, A., Axelsen, S., Van Den Dries, K., et al. (2010). Formulation of the Dutch Atmospheric Large-Eddy Simulation (DALES) and overview of its applications. *Geoscientific Model Development*, *3*(2), 415–444. https://doi.org/10.5194/gmd-3-415-2010

Hoffmann, F., Glassmeier, F., Yamaguchi, T., & Feingold, G. (2020). Liquid water path steady states in stratocumulus: Insights from process-level emulation and mixed-layer theory. *Journal of the Atmospheric Sciences*, *77*(6), 2203–2215. https://doi.org/10.1175/JAS-D-19-0241.1

Hoffmann, F., Glassmeier, F., Yamaguchi, T., & Feingold, G. (2023). On the roles of precipitation and entrainment in stratocumulus transitions between mesoscale states. *Journal of the Atmospheric Sciences*, *80*(12), 2791–2803. https://doi.org/10.1175/JAS-D-22-0268.1

Hoyer, S., & Joseph, H. (2017). xarray: N-D labeled Arrays and Datasets in Python. *Journal of Open Research Software*, *5*(1), 10. https://doi.org/10.5334/jors.148

Hunter, J. D. (2007). Matplotlib: A 2D graphics environment. *Computing in Science & Engineering*, *9*(3), 90–95. https://doi.org/10.1109/MCSE.2007.55

Janssens, M. (2023). *Mesoscale cloud patterns in the trade-wind boundary layer*. Doctoral dissertation. Wageningen University. https://doi.org/10.18174/635857

Janssens, M., De Arellano, J. V.-G., Van Heerwaarden, C. C., De Roode, S. R., Siebesma, A. P., & Glassmeier, F. (2023). Nonprecipitating shallow cumulus convection is intrinsically unstable to length scale growth. *Journal of the Atmospheric Sciences*, *80*(3), 849–870. https://doi.org/10.1175/JAS-D-22-0111.1

Janssens, M., Jansson, F., Alinaghi, P., Glassmeier, F., & Siebesma, P. (2024). Symmetry in mesoscale circulations explains weak impact of trade cumulus self-organisation on the radiation budget in large-eddy simulations. *EarthArXiv*. https://doi.org/10.31223/X5BH8Q

Janssens, M., Vilà-Guerau de Arellano, J., Scheffer, M., Antonissen, C., Siebesma, A. P., & Glassmeier, F. (2021). Cloud patterns in the trades have four interpretable dimensions. *Geophysical Research Letters*, *48*(5), e2020GL091001. https://doi.org/10.1029/2020GL091001

Jansson, F., Janssens, M., Grönqvist, J. H., Siebesma, A. P., Glassmeier, F., Attema, J., et al. (2023). Cloud botany: Shallow cumulus clouds in an ensemble of idealized large-domain large-eddy simulations of the trades. *Journal of Advances in Modeling Earth Systems*, *15*(11), e2023MS003796. https://doi.org/10.1029/2023MS003796

Jeevanjee, N., & Romps, D. M. (2013). Convective self-aggregation, cold pools, and domain size. *Geophysical Research Letters*, *40*(5), 994–998. https://doi.org/10.1002/grl.50204

Lamaakel, O., Venters, R., Teixeira, J., & Matheou, G. (2023). Computational domain size effects on large-eddy simulations of precipitating shallow cumulus convection. *Atmosphere*, *14*(7), 1186. https://doi.org/10.3390/atmos14071186

Langhans, W., & Romps, D. M. (2015). The origin of water vapor rings in tropical oceanic cold pools. *Geophysical Research Letters*, *42*(18), 7825–7834. https://doi.org/10.1002/2015GL065623

Li, Z., Zuidema, P., & Zhu, P. (2014). Simulated convective invigoration processes at trade wind cumulus cold pool boundaries. *Journal of the Atmospheric Sciences*, *71*(8), 2823–2841. https://doi.org/10.1175/JAS-D-13-0184.1

Lochbihler, K., Lenderink, G., & Siebesma, A. P. (2021). Cold pool dynamics shape the response of extreme rainfall events to climate change. *Journal of Advances in Modeling Earth Systems*, *13*(2), e2020MS002306. https://doi.org/10.1029/2020MS002306

Mapes, B. E. (2024). Evolutionary theory of convective organization. arXiv preprint arXiv:2404.03480. https://doi.org/10.48550/arXiv.2404.03480

Moncrieff, M. W., & Liu, C. (1999). Convection initiation by density currents: Role of convergence, shear, and dynamical organization. *Monthly Weather Review*, *127*(10), 2455–2464. https://doi.org/10.1175/1520-0493(1999)127⟨2455:CIBDCR⟩2.0.CO;2

Narenpitak, P., Kazil, J., Yamaguchi, T., Quinn, P., & Feingold, G. (2021). From sugar to flowers: A transition of shallow cumulus organization during atomic. *Journal of Advances in Modeling Earth Systems*, *13*(10), e2021MS002619. https://doi.org/10.1029/2021MS002619

Nissen, S. B., & Haerter, J. O. (2021). Circling in on convective self-aggregation. *Journal of Geophysical Research: Atmospheres*, *126*(20), e2021JD035331. https://doi.org/10.1029/2021JD035331

Nuijens, L., & Stevens, B. (2012). The influence of wind speed on shallow marine cumulus convection. *Journal of the Atmospheric Sciences*, *69*(1), 168–184. https://doi.org/10.1175/JAS-D-11-02.1

Nuijens, L., Stevens, B., & Siebesma, A. P. (2009). The environment of precipitating shallow cumulus convection. *Journal of the Atmospheric Sciences*, *66*(7), 1962–1979. https://doi.org/10.1175/2008jas2841.1

Radtke, J., Naumann, A. K., Hagen, M., & Ament, F. (2022). The relationship between precipitation and its spatial pattern in the trades observed during EUREC[4]A. *Quarterly Journal of the Royal Meteorological Society*, *148*(745), 1913–1928. https://doi.org/10.1002/qj.4284

Radtke, J., Vogel, R., Ament, F., & Naumann, A. K. (2023). Spatial organisation affects the pathway to precipitation in simulated trade-wind convection. *Geophysical Research Letters*, *50*(20), e2023GL103579. https://doi.org/10.1029/2023GL103579

Rochetin, N., Hohenegger, C., Touzé-Peiffer, L., & Villefranque, N. (2021). A physically based definition of convectively generated density currents: Detection and characterization in convection-permitting simulations. *Journal of Advances in Modeling Earth Systems*, *13*(7), e2020MS002402. https://doi.org/10.1029/2020MS002402

Rotunno, R., Klemp, J. B., & Weisman, M. L. (1988). A theory for strong, long-lived squall lines. *Journal of the Atmospheric Sciences*, *45*(3), 463–485. https://doi.org/10.1175/1520-0469(1988)045⟨0463:ATFSLL⟩2.0.CO;2

Ruppert, J. H., & Johnson, R. H. (2016). On the cumulus diurnal cycle over the tropical warm pool. *Journal of Advances in Modeling Earth Systems*, *8*(2), 669–690. https://doi.org/10.1002/2015MS000610

Savic-Jovcic, V., & Stevens, B. (2008). The structure and mesoscale organization of precipitating stratocumulus. *Journal of the Atmospheric Sciences*, *65*(5), 1587–1605. https://doi.org/10.1175/2007JAS2456.1

Schlemmer, L., & Hohenegger, C. (2016). Modifications of the atmospheric moisture field as a result of cold-pool dynamics. *Quarterly Journal of the Royal Meteorological Society*, *142*(694), 30–42. https://doi.org/10.1002/qj.2625

Schulz, H., Eastman, R., & Stevens, B. (2021). Characterization and evolution of organized shallow convection in the downstream North Atlantic trades. *Journal of Geophysical Research: Atmospheres*, *126*(17), e2021JD034575. https://doi.org/10.1029/2021JD034575

Seabold, S., & Perktold, J. (2010). Statsmodels: Econometric and statistical modeling with python. In *9th python in science conference*.

Seifert, A., & Heus, T. (2013). Large-eddy simulation of organized precipitating trade wind cumulus clouds. *Atmospheric Chemistry and Physics*, *13*(11), 5631–5645. https://doi.org/10.5194/acp-13-5631-2013

Stensrud, D. J., Coniglio, M. C., Davies-Jones, R. P., & Evans, J. S. (2005). Comments on "'a theory for strong long-lived squall lines' revisited". *Journal of the Atmospheric Sciences*, *62*(8), 2989–2996. https://doi.org/10.1175/JAS3514.1

Stevens, B., Bony, S., Brogniez, H., Hentgen, L., Hohenegger, C., Kiemle, C., et al. (2020). Sugar, gravel, fish and flowers: Mesoscale cloud patterns in the trade winds. *Quarterly Journal of the Royal Meteorological Society*, *146*(726), 141–152. https://doi.org/10.1002/qj.3662

Stevens, B., Bony, S., Farrell, D., Ament, F., Blyth, A., Fairall, C., et al. (2021). EUREC[4]A. *Earth System Science Data Discussions*, *13*(8), 1–78. https://doi.org/10.5194/essd-13-4067-2021

Tompkins, A. M. (2001). Organization of tropical convection in low vertical wind shears: The role of cold pools. *Journal of the Atmospheric Sciences*, *58*(13), 1650–1672. https://doi.org/10.1175/1520-0469(2001)058%3C1650:OOTCIL%3E2.0.CO;2

Torri, G., & Kuang, Z. (2019). On cold pool collisions in tropical boundary layers. *Geophysical Research Letters*, *46*(1), 399–407. https://doi.org/10.1029/2018GL080501

Torri, G., Kuang, Z., & Tian, Y. (2015). Mechanisms for convection triggering by cold pools. *Geophysical Research Letters*, *42*(6), 1943–1950. https://doi.org/10.1002/2015GL063227

Touzé-Peiffer, L., Vogel, R., & Rochetin, N. (2022). Cold pools observed during eurec 4 a: Detection and characterization from atmospheric soundings. *Journal of Applied Meteorology and Climatology*, *61*(5), 593–610. https://doi.org/10.1175/JAMC-D-21-0048.1

Vial, J., Vogel, R., & Schulz, H. (2021). On the daily cycle of mesoscale cloud organization in the winter trades. *Quarterly Journal of the Royal Meteorological Society*, *147*(738), 2850–2873. https://doi.org/10.1002/qj.4103

Virtanen, P., Gommers, R., Oliphant, T. E., Haberland, M., Reddy, T., Cournapeau, D., et al. (2020). SciPy 1.0: Fundamental algorithms for scientific computing in Python. *Nature Methods*, *17*(3), 261–272. https://doi.org/10.1038/s41592-019-0686-2

Vogel, R., Konow, H., Schulz, H., & Zuidema, P. (2021). A climatology of trade-wind cumulus cold pools and their link to mesoscale cloud organization. *Atmospheric Chemistry and Physics*, *21*(21), 16609–16630. https://doi.org/10.5194/acp-21-16609-2021

Vogel, R., Nuijens, L., & Stevens, B. (2016). The role of precipitation and spatial organization in the response of trade-wind clouds to warming. *Journal of Advances in Modeling Earth Systems*, *8*(2), 843–862. https://doi.org/10.1002/2015MS000568

Waskom, M. L. (2021). Seaborn: Statistical data visualization. *Journal of Open Source Software*, *6*(60), 3021. https://doi.org/10.21105/joss.03021

Weisman, M. L., & Rotunno, R. (2004). "A theory for strong long-lived squall lines" revisited. *Journal of the Atmospheric Sciences*, *61*(4), 361–382. https://doi.org/10.1175/1520-0469(2004)061(0361:ATFSLS)2.0.CO;2

Wes, M. K. (2010). Data structures for statistical computing in Python. In S. van der Walt & J. Millman (Eds.), *Proceedings of the 9th Python in Science Conference* (pp. 56–61). https://doi.org/10.25080/Majora-92bf1922-00a

Xue, H., Feingold, G., & Stevens, B. (2008). Aerosol effects on clouds, precipitation, and the organization of shallow cumulus convection. *Journal of the Atmospheric Sciences*, *65*(2), 392–406. https://doi.org/10.1175/2007JAS2428.1

Zuidema, P., Li, Z., Hill, R. J., Bariteau, L., Rilling, B., Fairall, C., et al. (2012). On trade wind cumulus cold pools. *Journal of the Atmospheric Sciences*, *69*(1), 258–280. https://doi.org/10.1175/JAS-D-11-0143.1

Zuidema, P., Torri, G., Muller, C., & Chandra, A. (2017). A survey of precipitation-induced atmospheric cold pools over oceans and their interactions with the larger-scale environment. *Surveys in Geophysics*, *38*(6), 1283–1305. https://doi.org/10.1007/s10712-017-9447-x